# Mechanics of defects in carbon nanotubes: Atomistic and multiscale simulations

Sulin Zhang,[1,*] Steven L. Mielke,[2] Roopam Khare,[1] Diego Troya,[2,†] Rodney S. Ruoff,[1] George C. Schatz,[2] and Ted Belytschko[1,‡]

[1]*Department of Mechanical Engineering, Northwestern University, 2145 Sheridan Road, Evanston, Illinois 60208-3111, USA*

[2]*Department of Chemistry, Northwestern University, 2145 Sheridan Road, Evanston, Illinois 60208-3113, USA*

Molecular mechanics (MM) calculations together with coupling methods bridging MM and finite crystal elasticity are employed to simulate the fracture of defected carbon nanotubes (CNTs) and to compare with the available experimental results. The modified second generation Brenner potential (MTB-G2) is adopted in the calculations. Our MM calculations show fair agreement with quantum mechanical (QM) benchmarks, and indicate that one- and two-atom vacancies reduce the fracture strength of CNTs by 20%–33% (whereas the QM calculations predict 14%–27%), but these fracture strengths are still much higher than the experimental data. We then demonstrate that this experimental and theoretical discrepancy can be attributed to the presence of large-scale defects, such as those that may arise from oxidative purification processes. Simulations on multiwalled CNTs and tubes twisted prior to tensile loading show negligible effects on the fracture strength, which indicates that these are not the causes of low experimental values. The effects of chirality and tube diameter on fracture strengths are also investigated.

## I. INTRODUCTION

Predicting the strength of carbon nanotubes (CNTs) is an interesting challenge from both the scientific and engineering viewpoints. From a scientific viewpoint, a CNT ostensibly offers a clean model for the study of fracture, since the fracture of a single molecule should involve only chemical bond breaking at the atomistic scale without other complications such as grain boundaries. From an engineering viewpoint, a thorough understanding of CNT fracture is needed for the design of CNT-reinforced composites. So far, comparisons of experimental data and theoretical calculations have manifested large discrepancies. According to the experimental measurements of Yu *et al.*,[1] the fracture strengths of 19 multiwalled CNTs (MWCNTs) ranged from 11 to 63 GPa with a mean value of 27.8 GPa (see Fig. 1). However, recent quantum mechanical (QM) calculations[2–7] for pristine tubes agree reasonably well with each other and indicate that the fracture of nanotubes is brittle at room temperature with a fracture stress in the range of 75–135 GPa depending on tube chirality. It is thus of interest to examine whether plausible defects or other possible effects stemming from the differences between the experiments and the numerical models could explain these discrepancies.

The cause of defects and their effects on the physical properties of CNTs have attracted considerable attention. One of the most intensively studied defects is the 5-7-7-5 dislocation formed by a Stone-Wales (SW) transformation.[8] It has been shown by QM calculations that the SW transformation is energetically favored above a tensile strain of about ∼5%–6% for armchair tubes[9,10] and ∼12% for zigzag tubes.[10] Aggregation of SW defects has been hypothesized to lead to crack initiation;[11] however, QM analysis[6] indicates that aggregations of SW defects do not markedly reduce the fracture strength of CNTs—at least at moderate temperatures where brittle failure mechanisms prevail. It was also noted[6] that empirical bond-order potentials[12] incorrectly predict such weakening, which suggests that these potentials must be used with caution when treating defected CNTs. Irradiation with energetic ions or electrons can knock carbon atoms out of the hexagonal lattice, producing single-atom or multiatom vacancies in CNTs.[13–15] Density functional theory (DFT) calculations showed that vacancy defects can form links between adjacent graphite layers,[16] providing a mechanism for improved intershell or intertube mechanical coupling.[17,18] In a recent study on the fracture of CNTs,[7] it was argued that large defects could be introduced in MWCNTs by oxidative purification processes.[19,20]

Due to the small size of CNTs, fracture experiments are extremely challenging, and measurements of the tensile failure strength of individual tubes are fairly limited.[1,21] QM calculations[2–7] have therefore been used to elucidate the fracture of CNTs; however, the computational cost limits QM studies to CNTs with relatively small dimensions. Molecular
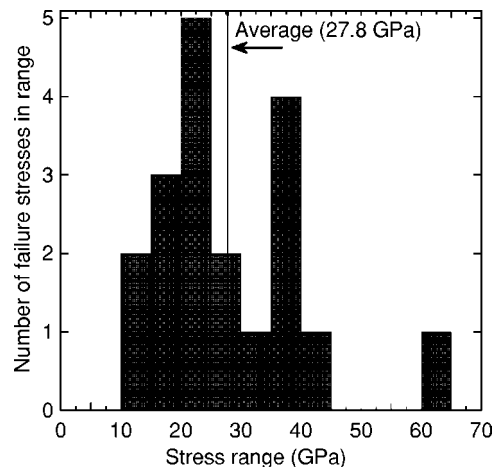


FIG. 1. Distribution of fracture stresses in the experiment of Yu *et al.* (Ref. 1).

dynamics (MD) and molecular mechanics (MM) calculations[7,22–26] using empirical potentials are computationally more affordable than QM calculations and have been widely adopted for modeling the fracture of CNTs. However, for MWCNTs or CNT bundles, even MM simulations are often quite time consuming.

For increased computational affordability, continuum models[27–29] of CNTs have become attractive substitutes for MM simulations. These models incorporate interaction potentials into the continuum constitutive laws by homogenization through the Cauchy-Born rule and can reproduce the corresponding atomistic models with reasonable accuracy for smooth deformations. Recently, a finite-element approach was developed in which nanotubes are treated as shells and the intershell van der Waals interactions are simulated by construction of special elements.[30] However, continuum methods alone are not adequate for failure analysis of CNTs.

The limitations of quantum mechanical and atomistic methods as well as continuum mechanics (CM) have stimulated extensive research into multiscale methods that bridge atomistic simulations and continuum descriptions.[31–35] The basic idea of multiscale methods is to use atomistic representations only in the localized region in which the positions of each individual atom are important and to use coarse-grained representations, such as finite-element methods, where the deformation is homogeneous and smooth. To ensure displacement compatibility between the two regions, most coupling methods have a "handshake region" or "transition region." Variations of the existing coupling methods stem from the detailed treatments of the handshake region. These aspects of multiscale methods are reviewed in detail elsewhere.[36–38] Multiscale methods have been applied to fracture,[34,39,40] grain-boundary interactions,[41] nanoindentation,[40,42] dislocation motion,[33,40,42,43] and localized deformation of CNTs.[44]

In this paper, we use MM and coupled MM/CM models to examine potential sources of discrepancies between the experiments[1] and available calculations, including the presence of single-atom and multi-atom vacancies, the presence of inner tubes that might give rise to intershell repulsive interactions, and twisting of the tubes prior to tensile loading. MM calculations optimize the configurations at zero temperature and thus do not include thermal effects; however, at room temperature, we expect that the effect of thermal contributions to the fracture strength of CNTs is negligibly small.

The paper is organized as follows: Section II gives an overview of the interaction potential, Sec. III details the MM scheme and the coupling method, Sec. IV presents the numerical results for the fracture strength of CNTs, and conclusions are given in Sec. V.

## II. INTERACTION POTENTIAL

Empirical potentials are generally used in MM and MD simulations to describe the interatomic interactions and have been incorporated into continuum constitutive laws through the Cauchy-Born rule. For nearly all empirical potentials, adjustable parameters are fitted based on various equilibrium

or near-equilibrium structures and configurations. Their application to tensile failure of defected CNTs, in which large distortions of chemical bonds occur, should thus be treated with caution. Belytschko *et al.*[23] adopted a modified Morse potential with an angle-bending term to simulate the fracture of CNTs with SW defects. The simplicity of this potential reduces the computational effort, but it is not able to accurately represent many-body interactions. A widely used bond-order potential for hydrocarbon systems is the Tersoff-Brenner form,[45–47] which has recently been revised with an extended database.[12] The revised second-generation Tersoff-Brenner potential (TB-G2) takes the form

$$E = \sum_i \sum_{j>i} f_c(r)[V^R(r_{ij}) - b_{ij}(\mathbf{r})V^A(r_{ij})], \qquad (1)$$

where $r_{ij}$ is the distance between atoms $i$ and $j$, $V^R$ and $V^A$ are the pairwise repulsive and attractive interactions, respectively, $b_{ij}$ is a bond-order function that has a complicated dependence on the bond angles and bond lengths involving atoms $i$ and $j$, and $f_c(r)$ is a cutoff function which reduces to zero interactions beyond 2.0 Å.

In some MM calculations using TB-G2, the predicted fracture stresses[22,24] are several times larger than those of the QM results. This is due to the functional form of the cutoff function in the potential, which artificially raises the bond force for distances between 1.7 Å and 2.0 Å.[6,23,48] To avoid nonphysical failure mechanisms, we follow a recommendation of Shenderova *et al.*[48] and remove this cutoff function, but include C-C interactions only for those atom pairs that are less than 2.0 Å apart in the initial, undeformed configurations.[6,23,48] We denote this modified potential as MTB-G2. With this modification, MTB-G2 is no longer capable of handling bond forming, but should give reasonable results for the fracture of CNTs.

## III. METHODOLOGY

In our numerical simulations, both MM and a coupled MM/CM method are employed to study the fracture of CNTs. The formulations and implementations of these two methods are described below.

### A. MM calculations

In the MM simulations, CNTs are uniaxially strained to fracture. At a given strain, the configuration is optimized using a conjugate-gradient (CG) method,[49] which yields a minimal potential energy configuration. The stress of the tube is obtained using finite differencing via

$$\sigma = \frac{E(l + \Delta) - E(l)}{\pi D t \Delta}, \qquad (2)$$

where $E(l)$ is the energy at length $l$, $\Delta$ is a finite stretch increment, $D$ is the diameter of the tube, and $t = 3.4$ Å is a nominal value for the thickness of CNTs (taken to be the interlayer spacing in graphite).

For convenience, both periodic and prescribed-displacement boundary conditions are considered in the MM calculations. CNTs are stretched by increasing the periodic
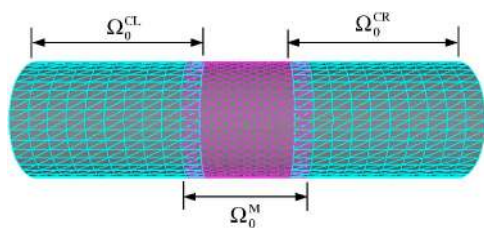
FIG. 2. (Color online) An illustration of the domain decomposition in the coupling method ($\Omega_0^C = \Omega_0^{CL} \cup \Omega_0^{CR}$ and $\Omega_0^O = \Omega_0^C \cap \Omega_0^M$).

length in the axial direction (when periodic boundary conditions are imposed) or by moving planes of edge atoms in opposite axial directions (when prescribed-displacement boundary conditions are imposed for finite-size CNTs). For pristine finite-size tubes, the edges are terminated with hydrogen atoms. In order to avoid edge fracture, periodic boundary conditions are applied in calculations of fracture of zigzag and armchair CNTs. For chiral CNTs, prescribed-displacement boundary conditions are imposed on hydrogen-capped finite-size tubes. We found that the fracture stresses of defected CNTs calculated with these two different boundary conditions are indistinguishable provided that the CNTs are sufficiently long. Therefore, in the following, boundary conditions are not distinguished.

### B. Coupling method

In the experiments of Yu *et al.*,[1] the diameters of the outer tubes range from 13 to 40 nm with an average of 25.4 nm. Modeling the fracture of these CNTs using MM calculations is computationally demanding. Here, the bridge-domain method recently developed by Belytschko and Xiao,[34] and used for simulating the fracture of graphene sheets, is extended to the three-dimensional case and employed to simulate the fracture of large-diameter single-walled CNTs (SWCNTs) and MWCNTs. This extension involves incorporating MTB-G2 into the continuum constitutive laws through the exponential Cauchy-Born rule,[27] as will be described later. A significant feature of this method is that in the "handshake" region the potential energy is a linear combination of the continuum and atomistic energies. This ensures a smooth bridging between continuum and atomistic deformation fields. The total energy of the coupled system is written as a weighted sum of the energies for the continuum and molecular regions, which allows minimizing the continuum and molecular configurations concurrently. This coupling scheme is advantageous since the finite-element meshes need not be graded down to the lattice spacing at the continuum-molecular interface, as is normally required by other methods.[31,33,39]

Figure 2 illustrates the domain decomposition for this method. The entire computational domain is decomposed into three regions: a molecular region $\Omega_0^M$, local to the defect; a continuum region $\Omega_0^C = \Omega_0^{CL} \cup \Omega_0^{CR}$, where the lattice undergoes homogeneous deformation; and the overlapping region $\Omega_0^O = \Omega_0^M \cap \Omega_0^C$, where the molecular and continuum models overlap. The size of the molecular region should be large enough so that the deformation in the region adjacent to

its boundary can be adequately represented by a continuum description. In the present set of calculations, the molecular region is at least 25 Å in length. In the following, we specify the potential energies for each region, which leads to the governing equations for the coupled system.

#### 1. Energy formulations

The energy of the coupled system is expressed as the sum of a covalent binding energy term and a nonbonded energy term. While the short-ranged covalent binding energy is spatially decoupled, the nonbonded energies arising from the long-ranged intershell interactions are coupled between the continuum and molecular regions. The formulations of these energy functions are described below.

a. *Covalent binding energy*. The covalent binding energy for the molecular region is a discrete sum of the interatomic potential energy terms as shown in Eq. (1), although the potential is not purely of a pairwise form due to the multidimensional character of the bond-order term. For the continuum region, the covalent binding energy is formulated within the framework of finite crystal elasticity. Generally, for space-filling crystalline materials, the standard Cauchy-Born rule establishes a link between the atomistic and the continuum descriptions, as

$$\mathbf{a} = \mathbf{F}\mathbf{A}, \qquad (3)$$

where $\mathbf{F}$ is the deformation gradient, and $\mathbf{A}$ and $\mathbf{a}$ are the lattice vectors in the undeformed and deformed configurations, respectively. However, when mapping a single-atom-thick crystalline film deforming in a three-dimensional space, the standard Cauchy-Born rule breaks down due to the fact that the lattice vectors in a curved surface are chords and are not tangent to the surface, while the deformation gradient $\mathbf{F}$ operates on vectors tangent to the surface. To overcome this conceptual drawback, an exponential Cauchy-Born rule was proposed,[27] as

$$\mathbf{a} = \mathcal{F}_X(\mathbf{A}), \qquad (4)$$

where $\mathcal{F}_X$ transforms the undeformed lattice vectors into a deformed one. Through a local approximation of the exponential map,[27] the deformed lattice vectors and the angles between two lattice vectors can be analytically represented in terms of the continuum deformation measures of the surface. Consider a representative unit cell of area $S_0$ containing two inequivalent nuclei and three inequivalent bonds in the reference, undeformed configuration. The hyperelastic strain-energy density $W$ can be formulated in terms of the MTB-G2 potential,

$$W = W[\mathbf{C}, \mathbf{K}, \eta] = \frac{1}{S_0} E_{\text{cell}} = \frac{1}{S_0} \sum_{i=1}^{3} \left[ V^R(\mathbf{a}_i) \right.$$
$$\left. + b(\mathbf{a}_i, \mathbf{a}_j, \mathbf{a}_k, \theta_j, \theta_k) V^A(\mathbf{a}_i) \right], \qquad (5)$$

where $\mathbf{C}$ and $\mathbf{K}$ are the stretch (the Green deformation tensor) and curvature tensors, respectively, $\mathbf{a}_i$, $\mathbf{a}_j$, and $\mathbf{a}_k$ are the three inequivalent bonds, $\theta_j$ and $\theta_k$ are the angles between these three bonds, $E_{\text{cell}}$ is the strain energy of the unit cell, and $S_0 = (3\sqrt{3}/2)\|\mathbf{A}\|^2$ is the area of the unit cell. Note that the

hexagonal lattice is a Bravais multi-lattice, so an additional kinematic variable $\eta$ must be introduced to describe the relative shift between the two basic lattices.[27–29] This inner variable is eliminated by minimizing the strain-energy density function, giving rise to a stable local lattice arrangement within the unit cell. After this inner relaxation, the strain-energy density can be written as a function of only **C** and **K**:

$$\hat{W} = W[\mathbf{C}, \mathbf{K}, \hat{\eta}[\mathbf{C}, \mathbf{K}]]. \tag{6}$$

Thus, the covalent binding energy for the continuum region that is subject to the deformation map $\phi$ that maps from undeformed to deformed configurations is

$$E_{cv}^{C} = \int_{\Omega_0^C} \hat{W}[\hat{\mathbf{C}}(\phi(\mathbf{X})), \hat{\mathbf{K}}(\phi(\mathbf{X}))]d\Omega_{0X}, \tag{7}$$

where **X** is a material point in the undeformed configuration.

b. *Nonbonded energy.* A Lennard-Jones (LJ) potential with parameters suggested by Girifalco *et al.*[50] is used to describe the intershell nonbonded interactions. The potential takes the form

$$V_{nb}(r) = \frac{\epsilon}{r_0^6}\left[\frac{1}{2}\kappa^6\left(\frac{r_0}{r}\right)^{12} - \left(\frac{r_0}{r}\right)^6\right], \tag{8}$$

where $r$ is an interatomic distance, $\kappa = 2.7$ is a dimensionless constant, $r_0 = 1.42$ Å is the equilibrium bond length, and $\epsilon = 15.2$ eV Å$^6$. A cutoff length of 6 Å for the LJ interaction is chosen for all simulations.

Homogenization of the discrete nonbonded energy between two unit cells gives rise to the van der Waals energy density

$$V_{nb}^{C-C}(r_{cc}) = \left(\frac{2}{S_0}\right)^2 V_{nb}(r_{cc}), \tag{9}$$

where $r_{cc}$ is the separation between two material points. Note that the factor of two on the right-hand side of Eq. (9) comes from the fact that each unit cell contains two nuclei. The nonbonded energy $E_{nb}^{C-C}$ over the continuum region is

$$E_{nb}^{C-C} = \frac{1}{2}\int_{\Omega_0^C}\int_{\Omega_0^C} V_{nb}^{C-C}[\|\phi(\mathbf{X}) - \phi(\mathbf{Y})\|]d\Omega_{0Y}d\Omega_{0X}, \tag{10}$$

where **Y** is another material point in the continuum region. The integration in Eq. (10) is evaluated in the entire continuum domain $\Omega_0^C$. Thus, in addition to the intershell nonbonded interactions, the intrashell nonbonded interactions are automatically included; however, in this work, the intrashell nonbonded interactions are neglected.

Similarly, the nonbonded energy density between a continuum point and an atom is obtained by homogenization of the nonbonded energy between an atom and a unit cell, as

$$V_{nb}^{C-A}(r_{mc}) = \frac{2}{S_0}V_{nb}(r_{mc}), \tag{11}$$

where $r_{mc}$ is the distance between the material point and the atom. The nonbonded energy between a set of atoms in $\Omega_0^M$ and the continuum region is
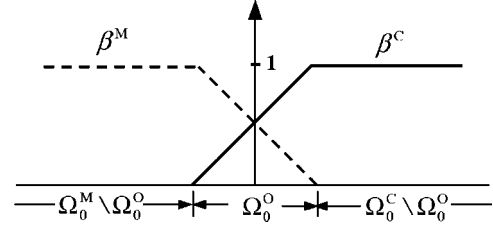


FIG. 3. The weight functions $\beta^M$ and $\beta^C$ in the three regions of the computational domain.

$$E_{nb}^{C-A} = \sum_{i \in \Omega_0^M}\int_{\Omega_0^C} V_{nb}^{C-A}[\|\phi(\mathbf{X}) - \mathbf{x}_i^m\|]d\Omega_{0X}, \tag{12}$$

where $\mathbf{x}_i^m$ is the position of atom $i$ in the deformed configuration.

### 2. Governing equations for the coupled system

The coupled problem is formulated by constructing the total potential energy. To avoid double counting the potential energy for the overlapping domain, the total energy of the coupled system, $E_{tot}$, is written as a weighted summation of the potentials of the three regions

$$E_{tot}[\phi, \varphi] = E_{cv} + E_{nb}, \tag{13}$$

where $\varphi = \{\mathbf{x}_i^m\}$,

$$E_{cv} = \sum_{i \in \Omega_0^M}\left[\beta^M\left(\frac{1}{2}(\mathbf{X}_i^m + \mathbf{X}_j^m)\right)\sum_{j>i} V_{ij}\right]$$
$$+ \int_{\Omega_0^C}\beta^C(\mathbf{X})\hat{W}[\hat{\mathbf{C}}(\phi(\mathbf{X})), \hat{\mathbf{K}}(\phi(\mathbf{X}))]d\Omega_{0X} \tag{14}$$

and

$$E_{nb} = \sum_{i \in \Omega_0^M}\sum_{j \in \Omega_0^M, j>i}\beta^M(\mathbf{X}_i^m)\beta^M(\mathbf{X}_j^m)V_{nb}^{M-M}(\|\mathbf{x}_i^m - \mathbf{x}_j^m\|)$$
$$+ \frac{1}{2}\int_{\Omega_0^C}\int_{\Omega_0^C}\beta^C(\mathbf{X})\beta^C(\mathbf{Y})V_{nb}^{C-C}[\|\phi(\mathbf{X})$$
$$- \phi(\mathbf{Y})\|]d\Omega_{0Y}d\Omega_{0X} + \sum_{i \in \Omega_0^M}\int_{\Omega_0^C}\beta^M(\mathbf{X}_i^m)\beta^C(\mathbf{X})$$
$$\times V_{nb}^{C-A}[\|\phi(\mathbf{X}) - \mathbf{x}_i^m\|]d\Omega_{0X}, \tag{15}$$

where $\mathbf{X}_i^m$ is the position of atom $i$ in the undeformed configuration, and $E_{cv}$ and $E_{nb}$ are the covalent binding energy and the nonbonded energy, respectively. The weight functions take the forms

$$\beta^C(\mathbf{X}) = 1 - \beta^M(\mathbf{X}) = \begin{cases} 1 & : \mathbf{X} \in \Omega_0^C \setminus \Omega_0^O, \\ \alpha & : \mathbf{X} \in \Omega_0^O, \\ 0 & : \mathbf{X} \in \Omega_0^M \setminus \Omega_0^O, \end{cases} \tag{16}$$

where the symbol "\" denotes the set-minus operation, and the parameter $\alpha$ varies linearly from 0 to 1 across the overlapping region, as seen in Fig. 3. The formulation in Eq. (15)

ensures that the system energy is reproduced from the corresponding atomistic model as long as the compatibility condition in the overlapping region is satisfied:

$$\phi(\mathbf{X}_i^m) = \mathbf{x}_i^m, \quad \text{for all } i \in \Omega_0^O, \qquad (17)$$

where $\phi(\mathbf{X}_i^m)$ can be regarded as the interpolation of the continuum deformation field at the atomic position $\mathbf{X}_i^m$. The constraints are realized by an augmented Lagrange multiplier method:

$$\Gamma[\boldsymbol{\phi}, \boldsymbol{\varphi}, \boldsymbol{\lambda}] = E_{\text{tot}}[\boldsymbol{\phi}, \boldsymbol{\varphi}] + \boldsymbol{\lambda}^T \cdot \mathbf{g} + \frac{1}{2} p \mathbf{g}^T \cdot \mathbf{g}, \qquad (18)$$

where $\boldsymbol{\lambda}$ is a vector of Lagrangian multipliers, $\mathbf{g}$ is a vector whose component is $g_i = \|\boldsymbol{\phi}(\mathbf{X}_i^m) - \mathbf{x}_i^m\|^2$ for all atoms $i \in \Omega_0^O$, and $p = 0.12$ eV Å$^{-3}$ is the penalty. Minimization of the functional $\Gamma$ with respect to $\boldsymbol{\phi}$ and $\boldsymbol{\varphi}$ gives rise to the equilibrium configurations for the continuum and atomistic regions, $\boldsymbol{\Phi}$ and $\boldsymbol{\Psi}$, respectively.

The finite-element approximation of $\boldsymbol{\Phi}$ was described elsewhere.[51] In simulating CNT fracture using the coupling method, the CNT is initially relaxed to the minimal-energy configuration that corresponds to its zero-strain state. Stretching or twisting is realized by displacing the finite-element nodes at the tube edges. At each prescribed displacement, the potential energy of the tubes is minimized, again by the CG method. The stress is computed by summing the forces over the nodes with the prescribed displacement. As will be shown later, this coupling method can reproduce the corresponding atomistic models reasonably well, but greatly reduces the number of unknowns in the nonlinear system of equations.

## IV. RESULTS AND DISCUSSION

In the experiments of Yu *et al.*,[1] arc-grown MWCNTs were used for the fracture tests. The MWCNTs were attached to two cantilevered atomic force microscopy (AFM) tips using carbonaceous material. It was experimentally observed that only the outermost shell was attached to the AFM tips, and only the outermost shell failed upon loading. Hence, we begin our numerical studies with the fracture of SWCNTs that represent the outer shells, followed by an assessment of the effect of the presence of inner shells in MWCNTs. Important aspects to be investigated include the energetics of defects, the dependence of fracture strength on defect size and configuration, on twisting of the tubes prior to uniaxial loading, and the effects of intershell mechanical coupling.

In our numerical examples, small-diameter SWCNTs are simulated by MM schemes, while MWCNTs and large-diameter SWCNTs are simulated using the coupling method. In stretching CNTs to fracture, the step size of the applied strain is 0.001 for both the MM and the coupled calculations. When the applied strain approaches the fracture strain, the step size is reduced to 0.00025. With this treatment, the calculated fracture strength is estimated to be accurate to within ±0.3 GPa.
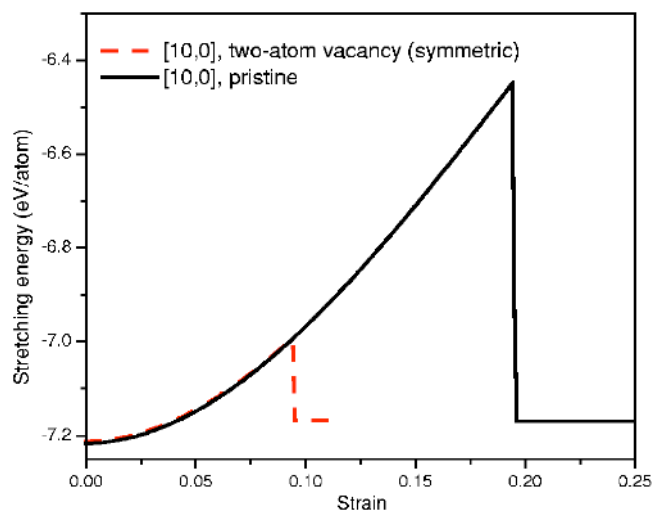


FIG. 4. (Color online) Stretching energy of a [10, 0] tube.

### A. Pristine CNTs

A pristine CNT does not present any preferred location for fracture nucleation. As a result, in a calculation, fracture often initiates simultaneously at several locations along the tube. Upon further stretching, the tube is segmented into several pieces, and the tube length chosen for the simulation appears to affect the number of segments. In the fracture process, the elastic strain energy is released, part of which becomes the surface energy (the energy associated with the newly created surfaces due to fracture). In practice, fracture occurs at only one place since the ideal symmetry of the numerical model does not occur at nonzero temperatures. To break the symmetry in the numerical model, one bond is slightly weakened. Specifically, the interaction force of this particular bond is taken to be 99.9% of the actual value calculated by MTB-G2. After introducing the weak bond, fracture initiates from that bond exclusively. This artifice, however, negligibly affects the fracture strength. Figure 4 (solid line) shows the energetics of a [10, 0] pristine tube under uniaxial stretching. The potential energy is a smooth parabola in the vicinity of the state of vanishing strain. At large strains, the potential energy curve deviates from parabolic, but remains smooth and indicates a nonlinear elastic stress-strain relationship since the curve is completely reversible without hysteresis. At a certain applied strain, the potential energy drops abruptly, corresponding to the occurrence of brittle fracture.

It is well known that graphene is isotropic in the regime of infinitesimal deformation, but anisotropic in finite deformations. CNTs, which are finitely deformed graphene sheets, should exhibit similar anisotropy. The elastic constants of CNTs show systematic variations with respect to tube chirality and diameter. Similarly, one expects anisotropy for the strength of CNTs. To confirm this strength anisotropy, a series of CNTs whose chiral angles ($\theta$) are approximately equally spaced between 0° (zigzag) and 30° (armchair), while having approximately the same diameter, are considered. Table I lists the CNTs, their diameters, and their chiral angles. Our simulations show a clear dependence of fracture

TABLE I. Chirality effects on the strength of CNTs (the defected CNTs contain a hole formed by removing a hexagonal unit and saturating dangling bonds with hydrogens) as predicted by MTB-G2.

| CNT | Diameter (Å) | Chirality ($\theta°$) | $\sigma_{cr}$ (pristine, GPa) | $\sigma_{cr}$ (defective, GPa) |
|---|---|---|---|---|
| [50, 0] | 39.16 | 0.0 | 88.3 | 57.2 |
| [47, 5] | 38.90 | 5.0 | 88.7 | 57.5 |
| [44, 10] | 38.96 | 10.0 | 89.4 | 57.6 |
| [40, 16] | 39.12 | 16.1 | 92.1 | 59.3 |
| [36, 21] | 39.10 | 21.4 | 95.7 | 62.6 |
| [33, 24] | 38.82 | 24.3 | 98.8 | 66.6 |
| [29, 29] | 39.32 | 30.0 | 105.3 | 77.5 |

strength on the chirality. The fracture strength monotonically increases with increasing $\theta$, with armchair tubes being ~19% stronger than zigzag tubes. This is substantially larger than what was noted[7] in our prior DFT (~5%) and PM3 (~9%) calculations, and even exceeds the factor of 15.5% that one would predict based on the higher density of axial bonds in armchair tubes as compared to zigzag tubes. The estimate $\sigma_{cr}(\theta) = \sigma_{cr}(\theta=0)/\cos\theta$ gives a good fit for small to intermediate values of $\theta$, but is too low by as much as ~3% for large $\theta$.

### B. Small vacancy defects

The removal of carbon atoms from the hexagonal network of the CNT creates a number of carbon atoms with unsaturated valence orbitals. The excess energy arising from the unsaturated valence orbitals promotes reconstructions local to the vacancy, forming energetically more stable configurations. We found that for the one- and two-atom vacancies, each has two possible reconstructed configurations, symmetric or asymmetric with respect to the axial direction of the CNT, as shown in Fig. 5. These reconstructions lead to dimensional changes local to the defects. Figure 6 shows the equilibrium configurations for two defective CNTs. For a two-atom vacancy (symmetric) in a [10, 0] tube, a dent appears near the defect. This defect affects the dimensions of the CNT only locally. For a two-atom vacancy (symmetric) in a [5, 5] tube, in addition to a local radius reduction, the tube is bent globally. These changes vanish upon stretching, so they have negligible effects on the fracture strength.

To understand the relative stability of these vacancy defects, the formation energies of the defects are calculated and listed in Table II. For a nanotube consisting of $n$ carbon atoms, the formation of vacancy defects involves taking carbon atoms out from the hexagonal lattice and possibly saturating dangling bonds with hydrogens, which can be expressed by

$$\frac{m}{2}H_2 + C_n = C_{n-k}H_m + kC(s, \text{graphite}). \quad (19)$$
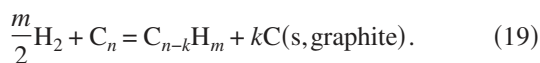
where the last term indicates that the removed carbon atoms are in their standard state, i.e., solid graphite. For the MTB-G2 potential, the covalent binding energy per atom of a graphene sheet and solid graphite is identical. Our

MTB-G2 calculations show that the formation energies for single and double vacancies in a graphene sheet are 7.14 eV and 8.18 eV, respectively, which are fairly close to DFT results[52] (7.4 eV and 8.7 eV for single and double vacancies, respectively). For the [10, 0] tube, the symmetric defect configuration is energetically more favorable than the asymmetric configuration, in contrast with the results for the [5, 5] tube. This indicates that vacancy reconstruction favors bond formation that is nearly transverse to the axial direction.

Figure 7 shows a set of stress-strain curves for [5, 5] CNTs under uniaxial tension obtained by MM and QM calculations; results are displayed for pristine tubes as well as for tubes containing a single vacancy defect. The semiempirical QM calculations using the PM3 method[53] are described elsewhere[7] and generally have higher accuracy than the MM
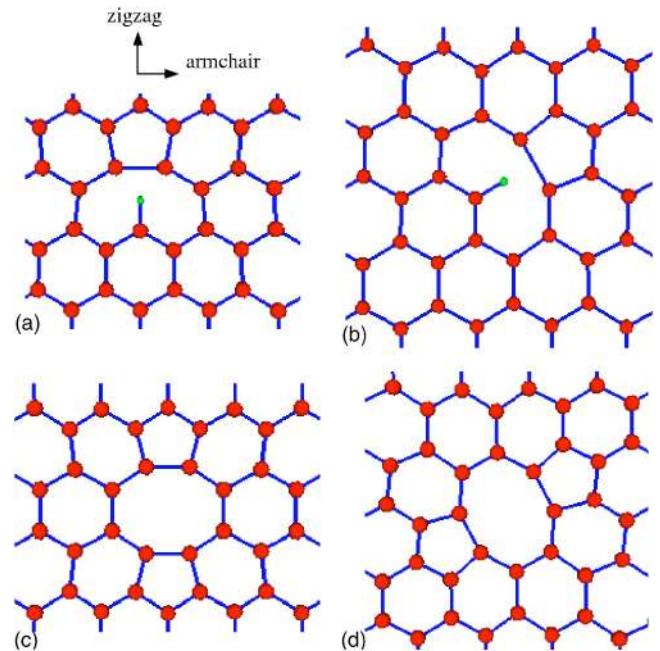


FIG. 5. (Color online) One- and two-atom vacancy defects (carbon large red dot; hydrogen, small green dot). (a) One-atom vacancy, symmetric [the axial directions for armchair and zigzag tubes are indicated, and are the same for (b), (c), and (d)]. (b) One-atom vacancy, asymmetric. (c) Two-atom vacancy, symmetric. (d) Two-atom vacancy, asymmetric. The single vacancy cases include a hydrogen to saturate the system.
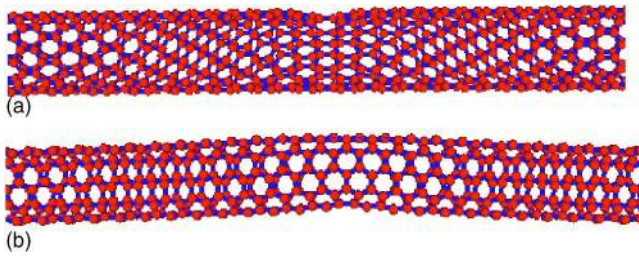
FIG. 6. (Color online) Equilibrium configurations of defective CNTs. (a) Two-atom vacancy (symmetric) in a [10, 0] CNT. (b) Two-atom vacancy (symmetric) in a [5, 5] CNT.

calculations. For comparison, the experimental data measured by Yu *et al.*[1] are also plotted. For pristine tubes the QM results are complicated by the existence of multiple fracture pathways; this is discussed in further detail in Ref. 7. MTB-G2 is observed to systematically underestimate both the Young's moduli and the fracture stresses. The discrepancies between the QM and MM calculations are even larger for the vacancy-defected CNTs than those for the pristine CNTs.

The fracture stresses and strains of a [5, 5] and a [10, 0] nanotube with one- and two-vacancy defects are summarized in Table II. The fracture stresses obtained by PM3 calculations are also included. For pristine tubes, the fracture stresses predicted by the MM calculations with the MTB-G2 potential are about 22% and 29% lower than those predicted by the QM calculations for the armchair and zigzag tubes, respectively. For the defected tubes, the difference in the fracture stresses predicted by these two calculations is up to ~40%. Fortunately, the agreement between the two methods is better for the fractional stress reductions (i.e., $1 - \sigma^{\text{defected}}/\sigma^{\text{pristine}}$), with MTB-G2 predicting weakening of between 20% and 33% (depending on the tube and defect type), whereas PM3 predicts weakening between 14% and 27%. Thus, although MTB-G2 greatly underestimates the absolute failure stresses, it only moderately overestimates the
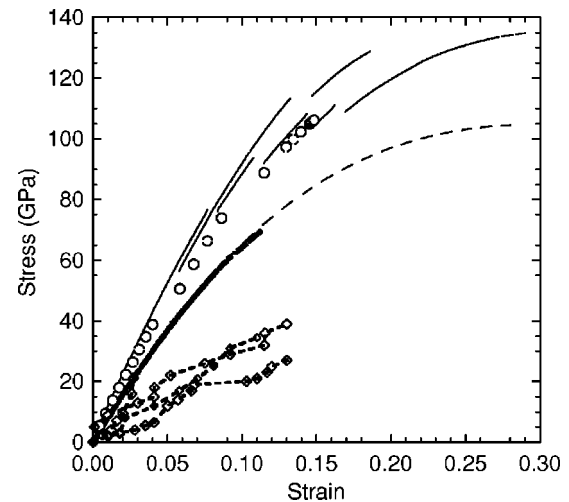


FIG. 7. Comparison of stress-strain curves of pristine and single vacancy defected [5, 5] CNTs obtained from QM and MM calculations. QM results for pristine tubes are indicated by solid lines. Circles indicate QM results for vacancy defected tubes. The long-dashed and dotted lines denote MM results for pristine and defected CNTs, respectively. The experimental results are indicated by diamonds connected by dashed lines. It should be noted that the experimentally measured strains are not reliable due to possible slippage at the cantilever-CNT attachments; however, this should not affect the measurements of the forces so the experimental failure stresses are still valid.

fractional stress reductions. The PM3 calculations predict that the fracture strength has a strong dependence on the defect orientation, with defects that reconstruct to form additional bonds that are more nearly axially aligned yielding stronger tubes. The MTB-G2 results do not accurately predict such variations.

The initial slopes (the Young's moduli) of the experimental stress-strain curves in Fig. 7 are only about 1/3 of the MM and QM results. As previously discussed,[23] these extremely low Young's moduli are likely due to slippage at the

TABLE II. Properties of vacancy defects, where $E_f$ represents defect formation energy, $\sigma_{\text{cr}}$ is the fracture stress, and $\varepsilon_{\text{cr}}$ is the fracture strain. The fracture stresses obtained by the PM3 method are listed in the last column, while numbers listed in the other columns are obtained using the MTB-G2 potential.

| Defect | $E_f$(eV) | $\sigma_{\text{cr}}$ (MM, GPa) | $\varepsilon_{\text{cr}}$ (%) | $\sigma_{\text{cr}}$ (PM3, GPa)[a] |
|---|---|---|---|---|
| [10, 0] pristine | - | 87.9 | 18.1 | 124 |
| [10, 0] sym., one-atom vac. +H | 2.7 | 64.7 | 8.6 | - |
| [10, 0] asym., one-atom vac. +H | 3.2 | 68.2 | 9.5 | - |
| [10, 0] sym., one-atom vac. | 5.2 | 64.8 | 8.6 | 101 |
| [10, 0] sym., two-atom vac. | 5.5 | 64.4 | 9.6 | 107 |
| [10, 0] asym., two-atom vac. | 5.9 | 64.8 | 10.9 | 92 |
| [5, 5] pristine | - | 105.5 | 29.7 | 135 |
| [5, 5] sym., one-atom vac. +H | 3.2 | 84.7 | 15.2 | 106 |
| [5, 5] asym., one-atom vac. +H | 2.7 | 70.9 | 11.5 | 99 |
| [5, 5] asym., one-atom vac. | 4.5 | 70.4 | 11.4 | 100 |
| [5, 5] sym., two-atom vac. | 5.5 | 71.3 | 11.7 | 105 |
| [5, 5] asym., two-atom vac. | 4.5 | 73.2 | 11.9 | 111 |

[a]Reference 7.

cantilever-CNT attachments in the experiments and are thus probably unreliable. However, slippage would not affect the measurement of the fracture strength in the experiments, so these should still be valid.

The stretching energetics of a [10, 0] tube with a two-atom vacancy (symmetric) is plotted in Fig. 4 (dashed line). Similar trends as are seen for pristine tubes are observed prior to fracture. For defected tubes, fracture initiates from the defects at a certain tensile strain. The axially-aligned C-C bonds in the ring of the tube that contains the defect then break simultaneously, creating a clean fracture surface.

### C. Large defects

The fracture strengths of CNTs with one- and two-atom vacancy defects obtained by the calculations reported in the preceding section are still much higher than the experimental failure stresses. One explanation[7] is that significantly larger defects may have been introduced in the CNTs used in the experiments. The MWCNTs used in the experiments of Yu *et al.*[1] were synthesized with a carbon arc apparatus.[19] The high temperatures involved leads to sintering of adjacent tubes[19,54,55]; thus, most of the tubes are highly defective. Oxidative etching using a stream of air at 650 °C for 30 min was used to burn away the vast majority of the product and a few seemingly well-formed tubes were then harvested. Oxidation of the soot and highly defected structures is very rapid, but even well-formed tubes might be expected to have an occasional vacancy defect, and these sites are also susceptible to damage. High-temperature oxidation of the basal plane of graphite by $O_2$ has been the subject of several studies,[54,56–60] and roughly circular pits in the surface graphene sheet are observed to rapidly form at the sites of vacancy defects. Solution phase purification treatments[20] involving strongly oxidizing acid baths together with sonication have also been suspected of etching holes in CNTs. Therefore, we explored the fracture of CNTs containing large defects of various configurations to see whether or not we obtain fracture stress values in the range found in the experiments.

Two types of defects are considered—holes and slits. The holes are intended to model the effects of oxidative pitting, and the slits are included due to their resemblance to cracks (although such structures are less likely to be experimentally significant). The slits are produced by removing a series of C-C atom pairs in the circumferential direction (bonded pairs alternating with nonbonded pairs). The hole defects, on the other hand, are created by removing hexagonal units. For example, the zero-level hole defect is created by removing an entire hexagonal unit; the first-level hole is created by removing another six hexagonal units centered around this hexagon. In each case, the dangling bonds of the edge carbons are saturated with hydrogen atoms. The higher-level holes are created by repeating this process. To make the results for the two defects (holes and slits) comparable, the length of the hole defect in the circumferential direction corresponds to the length of the slit defect at the same level. Note that the zero-level hole defect coincides with the zero-level slit defect. Figure 8 shows the hole and slit defects for
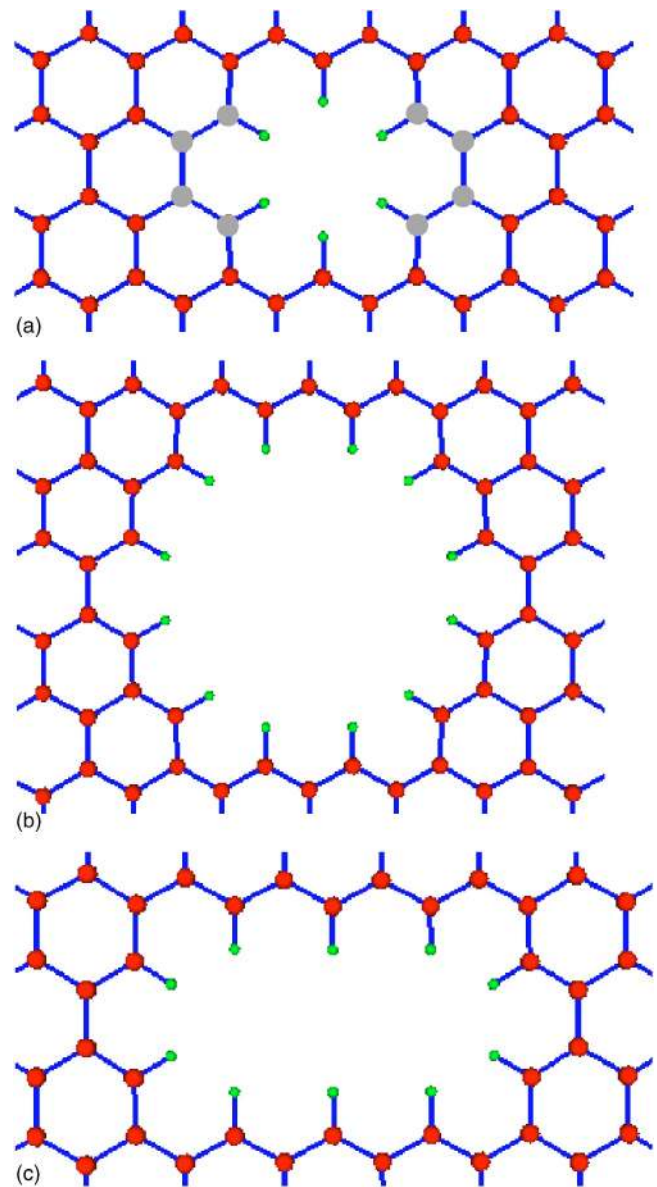


FIG. 8. (Color online) Hole and slit defects in CNTs (carbon, large red dot; hydrogen, small green dot). (a) The zero-level hole defect (also the zero-level slit defect), 6 carbon atoms are missing, dangling bonds are saturated by 6 hydrogen atoms. (b) The first-level hole defect, 24 carbon atoms are missing, dangling bonds are saturated by 12 hydrogen atoms. (c) The first-level slit defect created by removing the grey atoms in (a) and saturating dangling bonds with hydrogens; 14 carbon atoms are missing, dangling bonds are saturated by 10 hydrogens.

the first two levels.

Three CNTs [50, 0], [100, 0], and [29, 29] are considered. Comparison of the first two CNTs allows for diameter-dependence studies, while comparison between the [50, 0] and [29, 29] CNTs enables chirality-dependence analysis (the diameter of a [29, 29] is very close to that of a [50, 0] CNT). Figure 9 shows the variations of fracture stress with defect size (radius for hole defects and half-length for slit defects). As expected, the fracture stresses decrease monotonically with increasing defect sizes. The results also depend on the
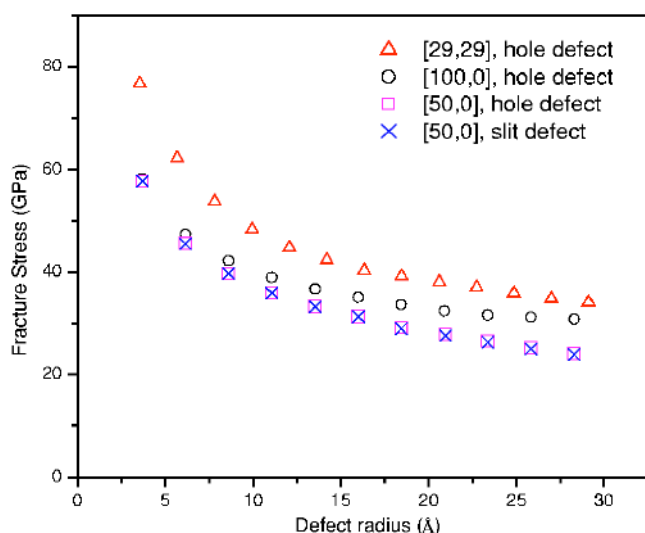
FIG. 9. (Color online) Dependence of fracture strength on defect size.



FIG. 10. (Color online) Variations of the radius of a [10, 0] pristine tube with the applied axial strain.

defect size relative to the tube diameter—for the smaller defect, the fracture stresses for the [50, 0] and [100, 0] tubes exhibit negligible differences; but as the defect size increases, these differences become progressively larger. This trend can be understood in terms of curvature effects. When the defect size is small relative to the diameter of the CNT, the CNT can locally be regarded as a flat graphene sheet; as the defect size increases and becomes comparable to the tube diameter, the curvature effect is no longer negligible. These trends are consistent with those observed in stress concentration factors for holes in thin-walled cylinders.[61] Our calculations show that the fracture stress is insensitive to whether the defect is a hole or a slit. For hole and slit defects of the same size, the fracture stresses differ by only ~1%.

The computed fracture strengths for CNTs with large defects are in the range of the experimental observations.[1] For the largest defect simulated here, the calculated fracture strengths are about 24 GPa, which is fairly close to the stress value with the maximum occurrence in the experimental data.[1] It is interesting to note that the reductions in strength obtained by the MM calculations agree reasonably well with the results of a new analytic model.[62]

The effect of chirality on the strength of defective CNTs was also studied. The zero-level hole defect was introduced to a series of tubes having similar radius and varying chiral angles. Curiously, as indicated in Table I, the presence of a hole reduces the fracture strengths of the first seven tubes by 33%–36%, but only weakens the armchair tube by 26%.

### D. Intershell mechanical coupling and twisting prior to loading

The previous simulations are all based on SWCNTs and thus neglect the effect of intershell van der Waals interactions in MWCNTs. Furthermore, during the attachment to the cantilevers, the CNTs may have been twisted or eccentrically loaded. These factors are studied here, and their effects on the fracture strength of CNTs are evaluated.
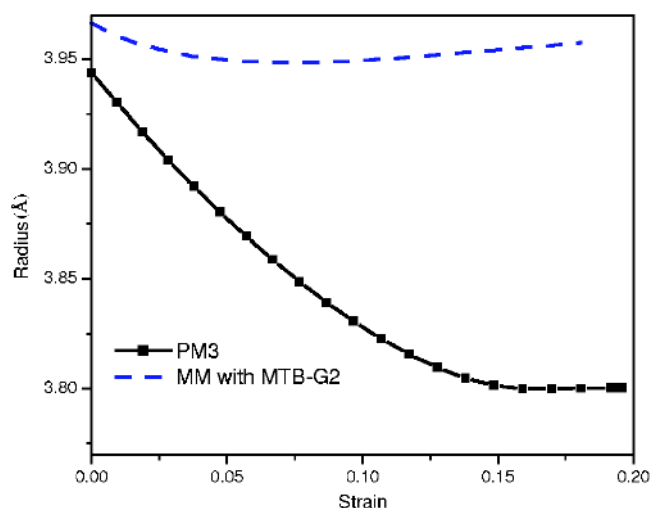
Under applied axial tension, nanotubes contract in the radial direction due to the Poisson effect. In a MWCNT, the radial contraction reduces intershell spacing, leading to increasing intershell interaction forces. MD calculations[63] using one of the first-generation Brenner potentials[47] reported that the Poisson's ratio of CNTs decreases monotonically with the applied axial strain. However, as seen from our calculations for a [10, 0] pristine CNT (see Fig. 10), MTB-G2 (and the unmodified TB-G2 potential) predicts that the nanotube radius expands when the applied axial strain is beyond 7.6%. This implies a negative tangential Poisson's ratio, which disagrees with the PM3 results (see Fig. 10) and the work[63] with earlier bond-order potentials.[47] The radial contraction of the [10, 0] tube just prior to fracture is 0.0088 Å, corresponding to a secant Poisson's ratio of 0.012. Thus, the intershell interaction forces are probably underestimated by MTB-G2. As a result, the effect of inner shells in a MWCNT, as will be presented below, may also be underestimated.

We first considered a [50, 0] SWCNT, a [50, 0]/[24, 24] double-walled CNT (DWCNT), and a [50, 0]/[24, 24]/[19, 19] triple-walled CNT (TWCNT). The SWCNT and the outer shells of the MWCNTs contain a two-atom vacancy (symmetric) [see Fig. 5(c)], while all the inner shells are defect free. The coupling method described earlier is employed to simulate the deformation of the CNTs. The SWCNT and the outer shells of the MWCNTs are represented by a MM/CM coupled model, while all the inner shells in the MWCNTs are treated by finite elements. In the simulation, only the outer shell is loaded, as the experiments clearly indicate that the outer shell is the only load-bearing one. The inner tubes evolve as determined by the intershell van der Waals interactions and are otherwise free of any constraints. Two loading conditions are considered. One is purely uniaxial tension. For the other, the tube is twisted to a certain angle, and then uniaxially stretched to fracture.

Figure 11 shows the stress-strain curves of the SWCNT and the DWCNTs subjected to uniaxial tension. For comparison, the stress-strain curve for the SWCNT computed by the
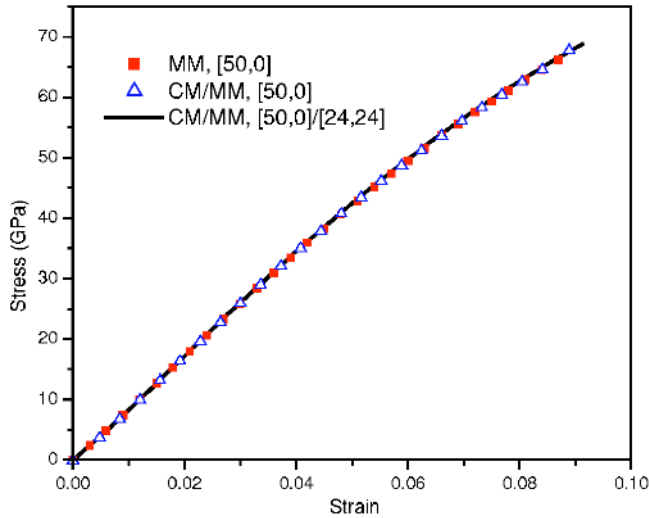
FIG. 11. (Color online) The stress-strain curves of a [50, 0] SWCNT and a [50, 0]/[24, 24] DWCNT subjected to uniaxial stretch. The outer shell contains a two-atom vacancy (symmetric), while the inner shell is defect free.

corresponding atomistic model is also included. It is shown that these curves are almost indistinguishable up to a large strain. The fracture strength obtained by the coupling method for the SWCNT is less than 2% larger than that from the atomistic model. This is likely due to the fact that the compatibility condition imposed in the overlapping region is not exactly satisfied in the coupling method. Compared with the fracture strength of the defected SWCNT, the fracture strengths of the DWCNT and TWCNT increase by around 1.3% and 1.5%, respectively. The fracture strengths of these CNTs are listed in Table III.

In evaluating the effects of twisting prior to tensile loading, the SWCNT and the MWCNTs are twisted by 5° and 15°, followed by uniaxial stretching to fracture. Figure 12 shows the configurations of the initially deformed tubes and those just prior to fracture. Upon twisting, the tubes are severely buckled, as shown in Figs. 12(a) and 12(c). For the DWCNT and TWCNT, the buckling is almost completely removed at strains just prior to fracture. In contrast, the SWNCT remains significantly distorted at all strains. Accordingly, the fracture strength of the SWCNT drops noticeably, while the fracture strengths of the DWCNT and TWCNT are only slightly reduced due to twisting, as shown

TABLE III. Effects on the fracture strength due to the presence of inner shells and twisting. Fracture of a SWCNT ([50, 0]) and MWCNTs ([50, 0]/[24, 24] and [50, 0]/[24, 24]/[19, 19]) are simulated. The outer shells of the MWCNT and the SWCNT contain a two-atom vacancy (symmetric) while all the inner shells are defect free.

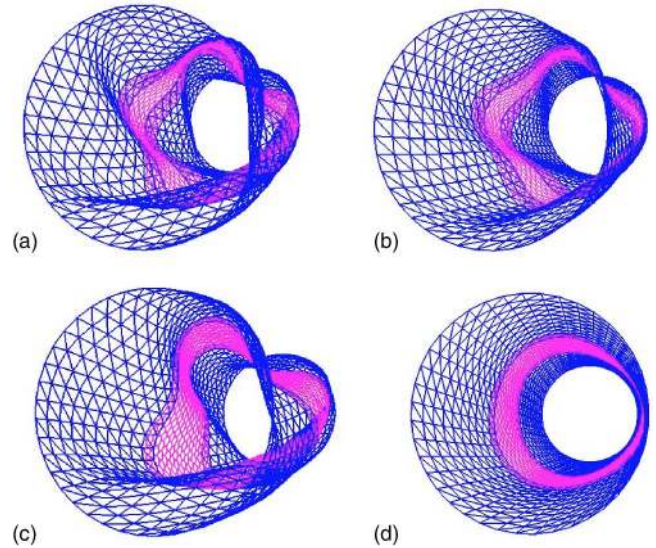| CNTs | $\sigma_{cr}$ (GPa, uniaxial) | $\sigma_{cr}$ (GPa, 5° twist) | $\sigma_{cr}$ (GPa, 15° twist) |
|------|-------------------------------|-------------------------------|--------------------------------|
| SWCNT | 67.8 | 67.1 | 64.8 |
| DWCNT | 68.7 | 68.6 | 68.1 |
| TWCNT | 68.8 | 68.7 | 68.2 |



FIG. 12. (Color online) Effect of twisting (15°) on the configurations for a [50, 0] SWCNT and a [50, 0]/[24, 24] DWCNT. For the DWCNT, only the outer shell is shown here. (a) SWCNT, unstretched. (b) SWCNT just prior to fracture. (c) Outer shell of the DWCNT, unstretched. (d) Outer shell of the DWCNT just prior to fracture.

in Table III. The 15° twist results in a smaller fracture strength than the 5° twist. We also considered situations where the top and bottom of the nanotubes were not perfectly aligned,—i.e., an eccentricity in the load. The effect on the fracture strength was again negligible.

The MWCNTs considered so far are significantly smaller than those in the experiments. Due to the Poisson effect, the absolute radial contraction upon stretching increases with increasing tube diameter. For instance, for a [50, 0] SWCNT at its fracture strain, its radial contraction is ~0.12 Å, while for a [338, 0] SWCNT at its fracture strain (9.6%), its radial contraction is ~0.78 Å. Note that the relationship between the radial contraction and tube diameter is nonlinear. For sufficiently large-diameter tubes, the radial contraction can be comparable to the intershell spacing (3.4 Å). As a result, for MWCNTs, the inner tube exerts a large hydrostatic pressure on the outer tube, which may affect the fracture strength. To study this effect, we considered five DWCNTs with increasing diameters. Table IV shows these fracture strengths of the DWCNTs. To illustrate the intershell mechanical coupling, the radial contractions of the inner and outer shells are listed, which are from the radius difference of the shells at the zero-strain state and the state just prior to fracture. It is shown that the radial contraction of outer tubes monotonically increases with increasing tube diameter, but not as much as that when the inner tubes are absent. The radial contraction of the inner tubes also monotonically increases and is only slightly smaller than the contraction of the outer shells. Overall, the fracture strength shows only a very small size effect, and the change of the magnitude is less than 1.5 GPa. Note, however, that the MTB-G2 potential underestimates the Poisson effect, and thus the effect of the presence of inner shells is also underestimated.

TABLE IV. Size effects on the fracture strength of DWCNTs. The outer tube contains a two-atom vacancy (symmetric), while the inner tube is defect free. $D_{outer}$ is the diameter of the outer tubes, and $\Delta R_{outer}$ and $\Delta R_{inner}$ are the radius decrements just prior to fracture as compared to the zero-strain state of the outer and inner tubes, respectively. The values for $\sigma_{cr}$ and $\Delta R_{outer}$ in parentheses correspond to the case when the inner shells are absent.

| CNTs | $D_{outer}$ (Å) | $\sigma_{cr}$ (GPa) | $\Delta R_{outer}$ (Å) | $\Delta R_{inner}$ (Å) |
|---|---|---|---|---|
| [50, 0]/[24, 24] | 39.15 | 68.7(67.8) | 0.07(0.12) | 0.03 |
| [71, 0]/[36, 36] | 55.59 | 68.8(68.3) | 0.10(0.13) | 0.07 |
| [116, 0]/[62, 62] | 90.83 | 69.3(68.8) | 0.17(0.24) | 0.14 |
| [220, 0]/[122, 122] | 172.26 | 69.6(69.1) | 0.32(0.42) | 0.26 |
| [388, 0]/[219, 219] | 303.80 | 70.1(69.4) | 0.50(0.78) | 0.43 |

## V. CONCLUDING REMARKS

Motivated by discrepancies between theoretical and experimental fracture strengths of CNTs, we studied the effects of vacancy defects, holes, and slits on fracture strength using MM and coupled MM/CM techniques. Where possible, these results are compared to available quantum mechanical calculations and fair agreement is observed. The MM calculations show that one- and two-atom vacancy defects weaken CNTs by 20%–33%, whereas QM calculations have shown 14%–27% reductions in strengths of these defects. The computed fracture strengths are slightly greater than the highest experimental values of Yu *et al.* and substantially greater than the average measured fracture strength. Holes (which may readily be introduced by oxidative purification processes) and slits (which are less likely to be experimentally relevant, but which have formal interest due to their resemblance to cracks) lower the fracture strength more significantly, falling in the upper range of the experimental observations. Slits and holes with a comparable cross section were observed to weaken tubes to a similar degree. The effect of tube chirality on fracture was explored; fracture strength increased monotonically with increasing chiral angle and armchair tubes were most resistant to the weakening effects of holes.

In addition to the MM calculations, calculations using a coupling method that bridges MM and finite crystal elasticity were presented. This coupling method enables the study of large-diameter SWCNTs and MWCNTs. Our simulations show that the presence of inner tubes only slightly increases the fracture strength of the CNTs considered, indicating small intershell mechanical coupling. Simulations of DWCNTs with two-atom vacancy defects in the outer shell show that the fracture strength is size dependent, but the variation is only a few GPa for the range of tube diameters considered. Twisting the tube prior to loading and other load imperfections were observed to negligibly affect the fracture strength of MWCNTs, but reduced the fracture strength of SWCNTs by as much as ~4% at a twisting angle of 15°. Therefore, imperfections in the loading are not a likely source of the low experimental fracture strengths.

---

*Electronic address: s-zhang6@northwestern.edu

†Current address: Department of Chemistry, Virginia Tech, 107 Davidson Hall, Blacksburg, VA, 24061-0212, USA.

‡Electronic address: tedbelytschko@northwestern.edu

[1] M.-F. Yu, O. Lourie, M. J. Dyer, K. Moloni, T. F. Kelly, and R. S. Ruoff, Science **287**, 637 (2000).

[2] T. Ozaki, Y. Iwasa, and T. Mitani, Phys. Rev. Lett. **84**, 1712 (2000).

[3] G. Dereli and C. Ozdogan, Phys. Rev. B **67**, 035416 (2003).

[4] T. Dumitrica, T. Belytschko, and B. I. Yakobson, J. Chem. Phys. **118**, 9485 (2003); **119**, 1281(E) (2003).

[5] S. Ogata and Y. Shibutani, Phys. Rev. B **68**, 165409 (2003).

[6] D. Troya, S. L. Mielke, and G. C. Schatz, Chem. Phys. Lett. **382**, 133 (2003).

[7] S. L. Mielke, D. Troya, S. Zhang, J.-L. Li, S. Xiao, R. Car, R. S. Ruoff, G. C. Schatz, and T. Belytschko, Chem. Phys. Lett. **390**, 413 (2004).

[8] A. J. Stone and D. J. Wales, Chem. Phys. Lett. **128**, 501 (1986).

[9] M. B. Nardelli, B. I. Yakobson, and J. Bernholc, Phys. Rev. B **57**, R4277 (1998).

[10] P. Zhang, P. E. Lammert, and V. H. Crespi, Phys. Rev. Lett. **81**, 5346 (1998).

[11] B. I. Yakobson, Appl. Phys. Lett. **72**, 918 (1998).

[12] D. W. Brenner, O. A. Shenderova, J. A. Harrison, S. J. Stuart, B. Ni, and S. B. Sinnott, J. Phys.: Condens. Matter **14**, 783 (2002).

[13] P. M. Ajayan, V. Ravikumar, and J.-C. Charlier, Phys. Rev. Lett. **81**, 1437 (1998).

[14] A. V. Krasheninnikov, K. Nordlund, M. Sirvio, E. Salonen, and J. Keinonen, Phys. Rev. B **63**, 245405 (2001).

[15] A. V. Krasheninnikov, K. Nordlund, and J. Keinonen, Phys. Rev. B **65**, 165423 (2002).

[16] R. H. Telling, C. P. Ewels, A. A. El-Barbary, and M. I. Heggie, Nat. Mater. **2**, 333 (2003).

[17] A. Kis, G. Csanyi, J.-P. Salvetat, T.-N. Lee, E. Couteau, A. J. Kulik, W. Benoit, J. Brugger, and L. Forro, Nat. Mater. **3**, 153 (2004).

[18] M. Huhtala, A. V. Krasheninnikov, J. Aittoniemi, S. J. Stuart, K. Nordlund, and K. Kaski, Phys. Rev. B **70**, 045404 (2004).

[19] D. T. Colbert, J. Zhang, S. M. McClure, P. Nikolaev, Z. Chen, J. H. Hafner, D. W. Owens, P. G. Kotula, C. B. Carter, J. H. Weaver, A. G. Rinzler, and R. E. Smalley, Science **266**, 1218 (1994).

[20] A. G. Rinzler, J. Liu, H. Dai, P. Nikolaev, C. B. Huffman, F. J. Rodriguez-Macias, P. J. Boul, A. H. Lu, D. Heymann, D. T. Colbert, R. S. Lee, J. E. Fischer, A. M. Rao, P. C. Eklund, and R. E. Smalley, Appl. Phys. A: Mater. Sci. Process. **67**, 29 (1998).

[21] B. G. Demczyk, Y. M. Wang, J. Cummings, M. Hetman, W. Han, A. Zettl, and R. O. Ritchie, Mater. Sci. Eng., A **334**, 173 (2002).

[22] B. I. Yakobson, M. P. Campbell, C. J. Brabec, and J. Bernholc, Comput. Mater. Sci. **8**, 341 (1997).

[23] T. Belytschko, S. P. Xiao, G. C. Schatz, and R. S. Ruoff, Phys. Rev. B **65**, 235430 (2002).

[24] Y. Hirai, S. Nishimaki, H. Mori, Y. Kimoto, S. Akita, Y. Nakayama, and Y. Tanaka, Jpn. J. Appl. Phys., Part 1 **42**, 4120 (2003).

[25] C. Wei, K. Cho, and D. Srivastava, Phys. Rev. B **67**, 115407 (2003).

[26] C. Wei, K. Cho, and D. Srivastava, Appl. Phys. Lett. **82**, 2512 (2003).

[27] M. Arroyo and T. Belytschko, J. Mech. Phys. Solids **50**, 1941 (2002).

[28] P. Zhang, Y. Huang, H. Gao, and K. C. Hwang, J. Appl. Mech. **69**, 454 (2002).

[29] P. Zhang, Y. Huang, P. Geubelle, P. A. Klein, and K. C. Hwang, Int. J. Solids Struct. **39**, 3893 (2002).

[30] A. Pantano, D. M. Parks, and M. C. Boyce, J. Mech. Phys. Solids **52**, 789 (2004).

[31] E. B. Tadmor, M. Ortiz, and R. Phillips, Philos. Mag. A **73**, 1529 (1996).

[32] F. F. Abraham, J. Q. Broughton, N. Bernstein, and E. Kaxiras, Comput. Phys. **12**, 538 (1998).

[33] L. E. Shilkrot, W. A. Curtin, and R. E. Miller, J. Mech. Phys. Solids **50**, 2085 (2002).

[34] T. Belytschko and S. P. Xiao, Int. J. Multiscale Comput. Eng. **1**, 115 (2003).

[35] G. J. Wagner and W. K. Liu, J. Comput. Phys. **190**, 249 (2003).

[36] W. A. Curtin and R. E. Miller, Modell. Simul. Mater. Sci. Eng. **11**, R33 (2003).

[37] N. M. Ghoniem, E. P. Busso, N. Kioussis, and H. Huang, Philos. Mag. **83**, 3475 (2003).

[38] W. K. Liu, E. G. Karpov, S. Zhang, and H. S. Park, Comput. Methods Appl. Mech. Eng. **193**, 1529 (2004).

[39] J. Q. Broughton, F. F. Abraham, N. Bernstein, and E. Kaxiras, Phys. Rev. B **60**, 2391 (1999).

[40] V. B. Shenoy, R. Phillips, and E. B. Tadmor, J. Mech. Phys. Solids **48**, 649 (2000).

[41] V. B. Shenoy, R. Miller, E. B. Tadmor, R. Phillips, and M. Ortiz, Phys. Rev. Lett. **80**, 742 (1998).

[42] J. Knap and M. Ortiz, Phys. Rev. Lett. **90**, 226102 (2003).

[43] L. E. Shilkrot, R. E. Miller, and W. A. Curtin, J. Mech. Phys. Solids **52**, 755 (2004).

[44] D. Qian, G. J. Wagner, and W. K. Liu, Comput. Methods Appl. Mech. Eng. **193**, 1603 (2003).

[45] J. Tersoff, Phys. Rev. Lett. **61**, 2879 (1988).

[46] J. Tersoff, Phys. Rev. B **39**, 5566 (1989); **41**, 3248(E) (1990).

[47] D. W. Brenner, Phys. Rev. B **42**, 9458 (1990); **46**, 1948(E) (1992).

[48] O. A. Shenderova, D. W. Brenner, A. Omeltchenko, X. Su, and L. H. Yang, Phys. Rev. B **61**, 3877 (2000).

[49] J. C. Gilbert and J. Nocedal, SIAM J. Optim. **2**, 21 (1992).

[50] L. A. Girifalco, M. Holak, and R. S. Lee, Phys. Rev. B **62**, 13 104 (2000).

[51] M. Arroyo and T. Belytschko, Int. J. Numer. Methods Eng. **59**, 419 (2004).

[52] A. A. Barbary, R. H. Telling, C. P. Ewels, M. I. Heggie, and P. R. Briddon, Phys. Rev. B **68**, 144107 (2003).

[53] J. J. P. Stewart, J. Comput. Chem. **2**, 209 (1989).

[54] X. K. Wang, X. W. Lin, V. P. Dravid, J. B. Ketterson, and R. P. H. Chang, Appl. Phys. Lett. **62**, 1881 (1993).

[55] P. Nikolaev, A. Thess, A. G. Rinzler, D. T. Colbert, and R. E. Smalley, Chem. Phys. Lett. **266**, 422 (1997).

[56] D. R. Olander, W. Siekhaus, R. Jones, and J. A. Schwarz, J. Chem. Phys. **57**, 408 (1972).

[57] R. T. Yang and C. Wong, Science **214**, 437 (1981).

[58] R. T. Yang and C. Wong, J. Chem. Phys. **75**, 4471 (1981).

[59] F. Stevens, L. A. Kolodny, and Thomas P. Beebe, Jr., J. Phys. Chem. B **102**, 10 799 (1998).

[60] S. M. Lee, Y. H. Lee, Y. G. Hwang, J. R. Hahn, and H. Kang, Phys. Rev. Lett. **82**, 217 (1999).

[61] H.-C. Wu and B. Mu, Composites, Part B **34**, 127 (2003).

[62] N. M. Pugno and R. S. Ruoff, Philos. Mag. **84**, 2829 (2004).

[63] K. Shintani and T. Narita, Surf. Sci. **532**, 862 (2003).